Transient growth of Ekman-Couette flow

Liang Shi,[1,2,*] Björn Hof,[1,3,†] and Andreas Tilgner[2,‡]
[1]*Max Planck Institute for Dynamics and Self-Organization, 37077 Göttingen, Germany*
[2]*Institute of Geophysics, University of Göttingen, 37077 Göttingen, Germany*
[3]*IST Austria, 3400 Klosterneuburg, Austria*
(Received 22 October 2013; published 6 January 2014)

Coriolis force effects on shear flows are important in geophysical and astrophysical contexts. We report a study on the linear stability and the transient energy growth of the plane Couette flow with system rotation perpendicular to the shear direction. External rotation causes linear instability. At small rotation rates, the onset of linear instability scales inversely with the rotation rate and the optimal transient growth in the linearly stable region is slightly enhanced $\sim \mathrm{Re}^2$. The corresponding optimal initial perturbations are characterized by roll structures inclined in the streamwise direction and are twisted under external rotation. At large rotation rates, the transient growth is significantly inhibited and hence linear stability analysis is a reliable indicator for instability.

DOI: 10.1103/PhysRevE.89.013001 PACS number(s): 47.52.+j, 47.20.Ft, 47.32.Ef

I. INTRODUCTION

Ekman-Couette flow represents the flow between two sliding parallel walls, where the whole setup is subject to external rotation around the axis perpendicular to the walls. Figure 1 shows schematically the geometry of the flow. In the extreme cases, the flow becomes either plane Couette flow (PCF) (if without rotation) or two well separated Ekman layers for large rotation rates. Because of the theoretical importance and the practical generality in planetary systems, these two canonical shear flows have both received an enormous amount of attention in the past decade and PCF under spanwise system rotation has also been widely studied [1,2]. However, little work has been done to study the Ekman-Couette flow. Hoffmann *et al.* [3] studied the secondary and tertiary flow states in Ekman-Couette flow, while Ponty *et al.* [4] investigated the onset of thermal convection between two shearing plates under the influence of external oblique rotation. Both studies focused mainly on the regime of moderate to large external rotation. Little attention has been paid to the instability at small rotation. Since experimental flows on earth are mostly subject to weak external rotation and the earth's rotation has been reported to have measurable influences in many other flows [5–8], the influence of weak system rotation on the Couette flows will be especially studied here.

In this paper we present a study on the linear stability and the transient energy growth exploring a wide parameter space in Ekman-Couette flow. This work is interesting theoretically and is also motivated by recent conflicting results [9–13] in astrophysical rotating flows on whether turbulence in cold accretion disks can arise via hydrodynamic instabilities. The Ekman layers introduced by the top and bottom end walls in experimental Taylor-Couette setups influence remarkably the bulk flow and make the flow rather complicated. In addition, the earth's rotation gives rise to another component of rotation, perpendicular to the rotation axis of the cylinders. At high Reynolds number Re, its effects may become non-negligible, except that the rotation axis of the cylinders aligns with the one of earth's rotation. We here choose the simplest geometry to study the influence of the Ekman layer on the linearly stable flows. We find that in PCF an infinitesimal external rotation causes linear instabilities.

This paper is structured in the following way. The linearized Ekman-Couette problem is formulated mathematically in Sec. II, followed by the linear stability analysis in Sec. III. We study the transient energy growth in Sec. IV.

II. PROBLEM FORMULATION

Considering that the fluid is incompressible, the governing equations of the fluid motion are the Navier-Stokes equations

$$\partial_t \mathbf{u} + \mathbf{u}\cdot\nabla\mathbf{u} + 2\Omega_0 \mathbf{e}_y \times \mathbf{u} = -\frac{1}{\rho}\nabla p + \nu\Delta\mathbf{u}, \quad \nabla\cdot\mathbf{u} = 0, \tag{1}$$

where $\mathbf{u}(\mathbf{x},t)$ is the flow velocity field and $p(\mathbf{x},t)$ is the pressure field. By taking the half gap distance between two plates $D/2$ as the length unit and $D/2U_0$ as the time unit,

$$l = l'D/2, \quad t = t'D/2U_0, \quad \mathbf{u} = \mathbf{u}'\cdot U_0, \quad p = p'\rho U_0^2,$$

we obtain the nondimensional form of Eq. (1),

$$\partial_t \mathbf{u} + \mathbf{u}\cdot\nabla\mathbf{u} + \frac{1}{\mathrm{Ro}}\cdot\mathbf{e}_y\mathbf{u} = -\nabla p + \frac{1}{\mathrm{Re}}\cdot\Delta\mathbf{u}, \quad \nabla\cdot\mathbf{u} = 0, \tag{2}$$

with the Reynolds number and the Rossby number

$$\mathrm{Re} = \frac{U_0 D}{2\nu}, \quad \mathrm{Ro} = \frac{U_0}{\Omega_0 D},$$

respectively. Note that the nondimensional symbols in Eq. (2) are omitted. We define another nondimensional parameter, the rotation number $\Omega = \frac{\Omega_0 D^2}{\nu}$. Here $\mathrm{Ro} = \frac{2\,\mathrm{Re}}{\Omega}$. Considering the boundary conditions and the symmetry property about the plane $y = 0$, the base velocity profile has the form of $[U(y),0,W(y)]$. We introduce the complex function

*liang.shi@ds.mpg.de
†bhof@ist.ac.at
‡andreas.tilgner@physik.uni-goettingen.de

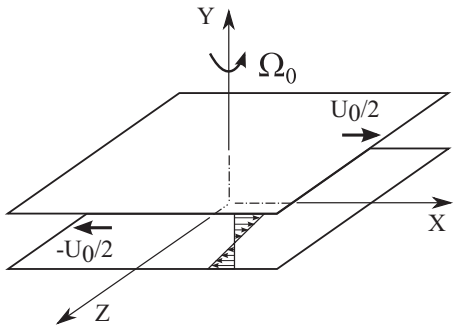

FIG. 1. Schematic of Ekman-Couette flow. The top and bottom walls both slide with velocity $U_0/2$, but in opposite directions along the X axis. The whole setup rotates at a speed of Ω_0 around the Y axis. The velocity profile corresponds to the base flow of plane Couette flow $[(U_0/2)y,0,0]$.

$Z(y) = U(y) + iW(y)$ and obtain

$$Z(y) = \frac{1}{2}\frac{e^{i\gamma y} - e^{-i\gamma y}}{e^{i\gamma} - e^{-i\gamma}}, \tag{3}$$

with $\gamma = \sqrt{\frac{\mathrm{Re}}{\mathrm{Ro}}}\frac{1+i}{\sqrt{2}}$. Figure 2 displays the base velocity profile at $\mathrm{Re} = 1000$, with and without rotation, respectively. At $\Omega = 50$, the external rotation distorts qualitatively the base flow such that the inflection points appear in the profiles.

To study the linear stability and transient dynamics of the base flow, we decompose the velocity field as $\mathbf{u} = \mathbf{u}_{\mathrm{pert}} + \mathbf{U}_{\mathrm{base}}$, where $\mathbf{U}_{\mathrm{base}} = [U(y),0,W(y)]$. Let v and η denote the perturbation of the wall-normal velocity and vorticity. By taking the curl of Eq. (2) once and twice, respectively, and then projecting into the Y direction, we obtain the linearized equations for the perturbation variables (v,η),

$$\begin{aligned}
&\partial_t \nabla^2 v + (U\partial_x + W\partial_z)\nabla^2 v - W''\partial_z v - U''\partial_x v \\
&\quad = \frac{1}{\mathrm{Re}}\nabla^4 v - \frac{1}{\mathrm{Ro}}\partial_y \eta, \\
&\partial_t \eta + (U\partial_x + W\partial_z)\eta + U'\partial_z v - W'\partial_x v \\
&\quad = \frac{1}{\mathrm{Re}}\nabla^2 \eta + \frac{1}{\mathrm{Ro}}\partial_y v.
\end{aligned} \tag{4}$$

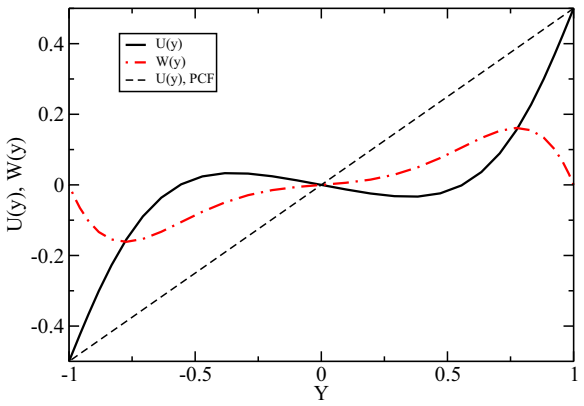

FIG. 2. (Color online) Base velocity profiles at $\mathrm{Re} = 1000$, $\Omega = 50$ (solid and dash-dotted lines) and at $\mathrm{Re} = 1000, \Omega = 0$ (dashed line).

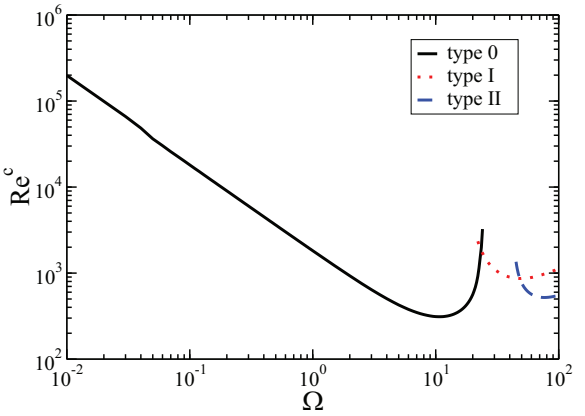

FIG. 3. (Color online) Critical Reynolds number Re^c as a function of Ω. For $\Omega < 5$, the critical Re scales inversely with the system rotation $\mathrm{Re}^c \simeq 1800\ \Omega^{-1}$.

In this paper we focus on the following modal perturbation:

$$v = \hat{v}(y,t)e^{i(\alpha x+\beta z)}, \quad \eta = \hat{\eta}(y,t)e^{i(\alpha x+\beta z)},$$

where α and β are the wave numbers in the X and Z directions, respectively. By inserting into Eq. (4), we have the modal

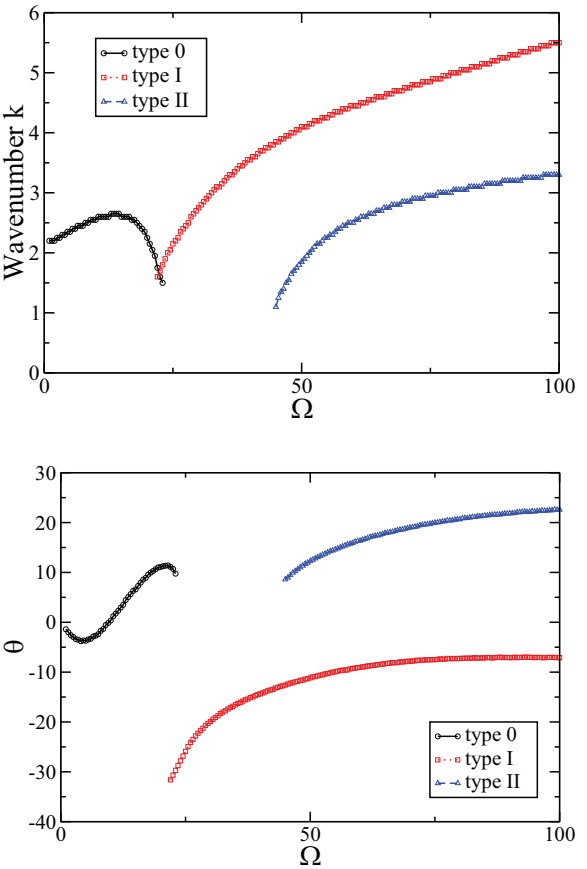

FIG. 4. (Color online) Variation with Ω of the wave number $k = \sqrt{\alpha^2 + \beta^2}$ (top) and the angle θ (bottom).

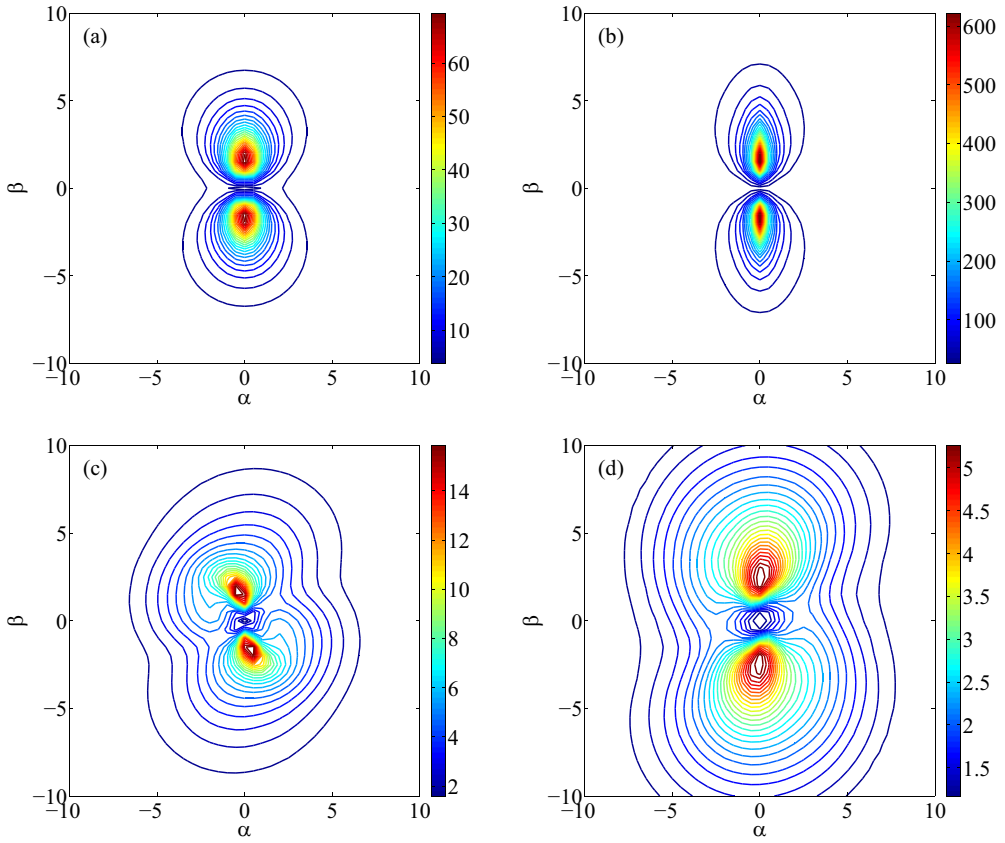

FIG. 5. (Color online) Contour plot in (α,β) space of the global maximum growth rate G^m: (a) $\mathrm{Re}=500,\Omega=0.05$; (b) $\mathrm{Re}=1500$, $\Omega=0.050$; (c) $\mathrm{Re}=500,\Omega=20$; and (d) $\mathrm{Re}=500,\Omega=50$. The size of G^m is indicated by the color value.

equations

$$\begin{aligned}\partial_t\hat{\nabla}^2\hat{v} &= -i(U\alpha+W\beta)\hat{\nabla}^2\hat{v}+i(U''\alpha+W''\beta)\hat{v}\\ &\quad+\frac{1}{\mathrm{Re}}\hat{\nabla}^4\hat{v}-\frac{1}{\mathrm{Ro}}\partial_y\hat{\eta},\\ \partial_t\hat{\eta} &= -i(U\alpha+W\beta)\hat{\eta}-i(U'\beta-W'\alpha)\hat{v}\\ &\quad+\frac{1}{\mathrm{Re}}\hat{\nabla}^2\hat{\eta}+\frac{1}{\mathrm{Ro}}\partial_y\hat{v},\end{aligned}\tag{5}$$

with $\hat{\nabla}^2=\partial_y^2-(\alpha^2+\beta^2)$.

Through the Chebyshev spectral discretization in the spatial direction [14], the above partial differential equations are transformed into a linear system $\partial_t\hat{\mathbf{v}}=-iL\hat{\mathbf{v}}$, where $\hat{\mathbf{v}}=[\hat{v},\hat{\eta}]$. The linear stability and transient growth are then calculated by the eigenvalues and eigenvectors of the linear operator L, which is computed in this paper by the subroutines in the LAPACK library. The accuracy and convergency of the method have been verified against the results in [14].

III. LINEAR INSTABILITY

The inflection points in the base profile hint that the Ekman-Couette flow may be linearly unstable. Thus we first investigate the linear instability of the flow. The ranges of parameters under study are $\mathrm{Re}\in[100,300\,000]$ and $\Omega\in[0,100]$. A bisection method is employed to find the critical curve $\mathrm{Re}^c(\Omega)$, separating the linearly stable and unstable regions. The results are shown in Fig. 3. At small Ω ($\Omega<5$), the linear instability is here referred to as type 0 and the critical Reynolds number Re^c is found to scale with Ω as $\mathrm{Re}^c(\Omega)\simeq 1800\,\Omega^{-1}$. Therefore, as $\Omega\to 0$, $\mathrm{Re}^c\to\infty$, which is consistent with the linear stability of plane Couette flow ($\Omega=0$) at any Re [15,16]. As Ω is increased, we recover the type I and type II instabilities previously found in Ekman layer flow [17]. The corresponding wave numbers are shown in Fig. 4. Here the wave number $k=\sqrt{\alpha^2+\beta^2}$ and the angle $\theta=-\arctan(\alpha/\beta)$, where θ is the angle between the wave vector $\mathbf{k}$ and the Z axis. The negative sign indicates the counterclockwise direction. As shown in Fig. 4, type I instability is characterized by a large wave number and a negative angle, while type II has a smaller wave number and a positive angle. The results agree very well with the ones previously reported in [3,4].

IV. TRANSIENT GROWTH

Below the neutral stability curve $\mathrm{Re}^c(\Omega)$, the flow is linearly stable and the transient growth of initial perturbations may play an important role in the nonlinear transition to turbulence. Due to the non-normality of the governing linear operator L, PCF undergoes substantial transient growth before nonlinear interaction sets in [14,18]. However, the influence of the external system rotation on the transient behavior is still

unknown. Here we employ the method presented in [14] to compute the optimal transient growth and the optimal perturbations. Let us first define the physical quantities of interest, the spectral energy

$$\hat{E}(\alpha,\beta,\mathrm{Re},\Omega;t) = \|\hat{\mathbf{v}}\|^2 = \int_{-1}^{1} (|\partial_y \hat{v}|^2 + k^2|\hat{v}|^2 + |\hat{\eta}|^2) dy \tag{6}$$

and the optimal growth function

$$G(\alpha,\beta,\mathrm{Re},\Omega;t) = \sup_{\hat{\mathbf{v}}(\cdot;0)\neq 0} \frac{\hat{E}(\cdot;t)}{\hat{E}(\cdot;0)} = \sup_{\hat{\mathbf{v}}(\cdot;0)\neq 0} \frac{\|\hat{\mathbf{v}}(\cdot;t)\|}{\|\hat{\mathbf{v}}(\cdot;0)\|}. \tag{7}$$

The spectral energy measures the kinetic energy contained in the mode (α,β), while the optimal growth function is the maximal energy growth achievable among all possible initial perturbations within time t. As presented in [14], the growth function $G(\cdot;t)$ can be directly computed by the eigenvalues and eigenvectors of the linear operator L. For simplicity of notation, we introduce two additional functions: the maximal growth in time as $G^m(\alpha,\beta,\mathrm{Re},\Omega) = \max_t G(\alpha,\beta,\mathrm{Re},\Omega;t)$ and the global optimal growth in the (α,β) plane as $G^{\mathrm{opt}}(\mathrm{Re},\Omega) = \max_{\alpha,\beta} G^m(\alpha,\beta,\mathrm{Re},\Omega)$. One property of G^m is the symmetry under the transformation $(\alpha \to -\alpha, \beta \to -\beta)$. The maximal growth G^m in the α-β plane at various Re and Ω is shown in Fig. 5, evidencing the symmetry with respect to the point $(0,0)$. The Reynolds number and the rotation number are fixed in each case. The range in the α-β plane is $[-10,10]\times[-10,10]$. At small Ω [Fig. 5(a)], the contour plot of G^m is similar to that in plane Couette flow [14], where the maximum is located very close to the β axis. As Ω increases, the effect of the external rotation becomes non-negligible and the maximum moves away from the β axis. Moreover, increasing Re from 500 [Fig. 5(a)] to 1500 [Fig. 5(b)] results in a substantial increase of G^m, while increasing Ω from 0.05 [Fig. 5(a)] to 50 [Fig. 5(d)] leads to a sharp decrease in G^m. It is worth noting that the modes that achieve the maximal transient growth are not the least unstable modes computed from the linear stability analysis.

We further compute the global optimal growth function $G^{\mathrm{opt}}(\mathrm{Re},\Omega)$ in the linearly stable region in $\mathrm{Re}\in[0,100]$ and $\Omega\in[0,1500]$. The search for the global maximum in the α-β plane is done by the downhill simplex method [19]. Figure 6 shows the contour plot of $G^{\mathrm{opt}}(\mathrm{Re},\Omega)$. The highest growth is located in the top left region with low Ω and high Re, while the lowest growth is in the bottom right region with high Ω and low Re. Nevertheless, the middle bumps in the contour plot show that the growth variation is not monotonic, whereas the nonsmooth irregular patches are due to the lack of sufficiently high resolution. Quantitatively, the scaling of G^{opt} with Re and Ω is shown in Fig. 7. Figure 7(a) displays the variation of $G^{\mathrm{opt}}(\mathrm{Re},\Omega)$ with Re at fixed Ω. The optimal growth scales at small Ω slightly faster than a power law with Re, $G^{\mathrm{opt}} \sim \mathrm{Re}^2$, whereas the power-law scaling disappears at large Ω and the transient growth becomes much smaller than the one at small Ω. Figure 7(b) plots the growth G^{opt} as a function of Ω when Re is fixed. It can be seen that the transient growth is enhanced with weak external rotation, while it is dramatically suppressed as $\Omega > 25$.

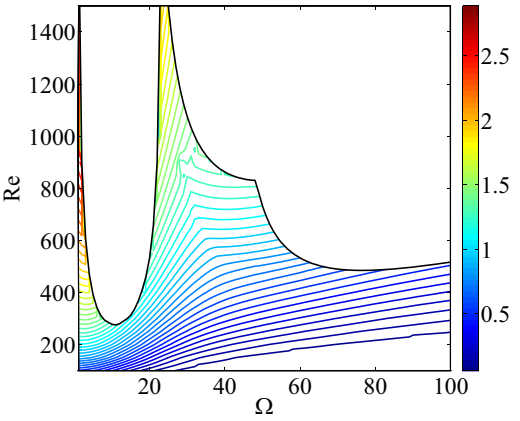

FIG. 6. (Color online) Contour plot of the global optimal growth G^{opt} in the Ω-Re plane. The boundary (black line) is the neutral curve from the linear stability analysis. The color value is on a logarithmic scale, e.g., the value 2 denotes $G^{\mathrm{opt}} = 10^2$.

The transient growth in rotating Couette flow is finally compared to the case without external rotation. Here in the rotating case we choose $\Omega = 0.05$. For a plane Couette setup in Göttingen with a gap distance $D \simeq 0.03$ m, the rotation number induced by the earth's

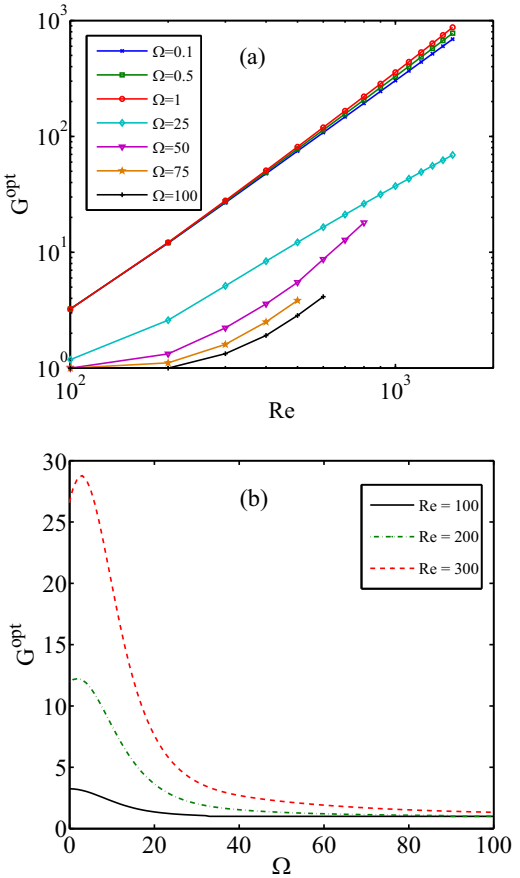

FIG. 7. (Color online) Scaling of G^{opt} with (a) Re at different Ω and (b) Ω at different Re.

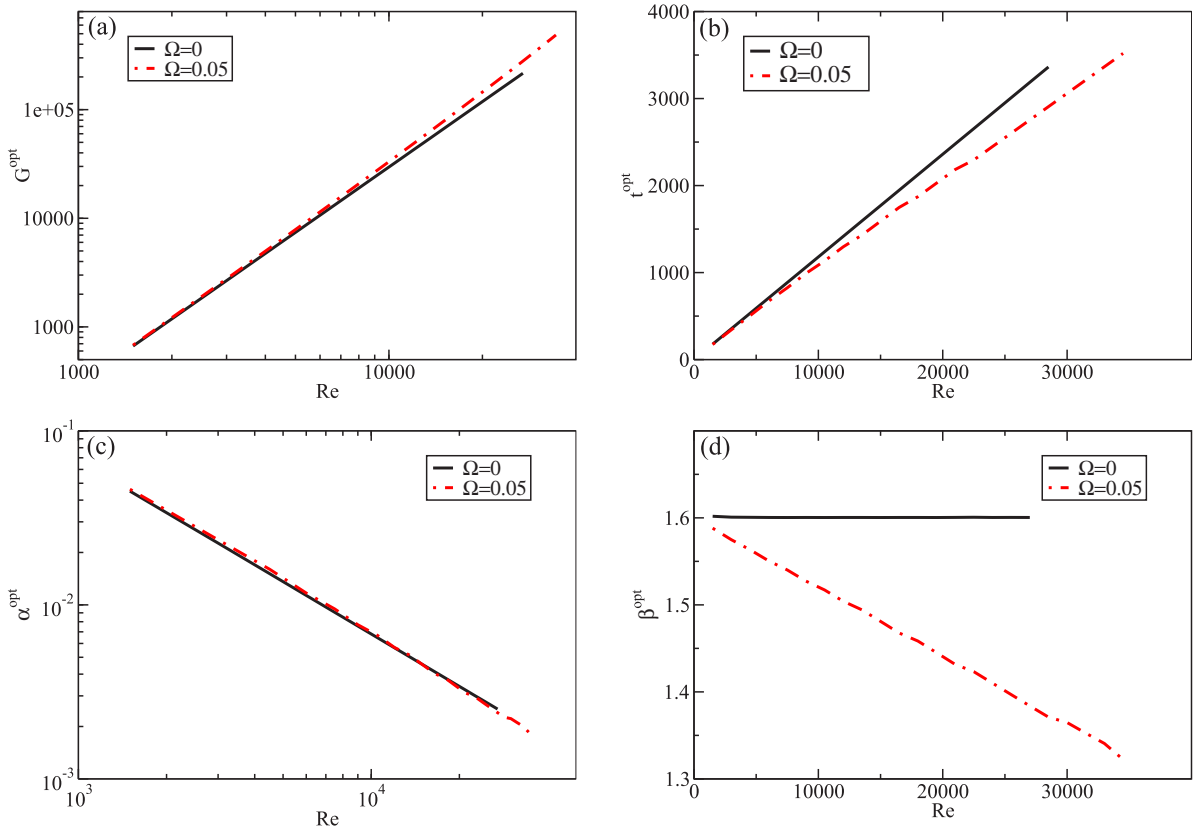

FIG. 8. (Color online) Scaling with Reynolds number at $\Omega = 0$ and 0.05: (a) global mamixum $G^{\text{opt}} \sim \text{Re}^{-2}$; (b) corresponding time when the global maximum is attained, $t^{\text{opt}} = a + b\,\text{Re}$; (c) wave number $\alpha^{\text{opt}}(\text{Re}) \sim \text{Re}^{-1}$, which is almost the same at different Ω; and (d) wave number $\beta^{\text{opt}}(\text{Re}) = c + d\,\text{Re}$, with different slopes at different Ω.

rotation $\Omega_0 \simeq 7.3 \times 10^{-5}\sin(51.32\pi/180) \simeq 5.7 \times 10^{-5}$ is $\Omega = \frac{\Omega_0 D^2}{\nu_{H_2O}} \simeq 0.0513$, where the water viscosity is $\nu_{H_2O} \simeq 10^{-6}\,\text{m}^2/\text{s}$ at $T = 20^\circ$. The Reynolds number under investigation is in the range $\text{Re} \in [1500, 35\,000]$. The results are plotted in Fig. 8. In PCF, we have the optimal transient growth $G^{\text{opt}} \simeq 1.18 \times 10^{-3}\text{Re}^2$ [Fig. 8(a)] achieved at time $t^{\text{opt}} \simeq 0.117\,\text{Re}$ [Fig. 8(b)], which agrees perfectly with the results in [18]. The corresponding wave number α^{opt}, as shown in Fig. 8(c), scales as $\alpha^{\text{opt}} \sim \text{Re}^{-1}$ and β^{opt} [Fig. 8(d)] stays constant, $\beta^{\text{opt}} \simeq 1.60$. For the case with external rotation $\Omega = 0.05$, the transient growth is slightly increased, with a power exponent a little greater than 2.0, which is obtained at an earlier moment [see Fig. 8(b)]. The wave number α is basically the same as the case without rotation, while the wave number β decreases linearly with Re and has a different slope at different Ω. Furthermore, as shown in Fig. 9, both optimal perturbations are in the form of inclined roll structures. However, the elongated rolls in the case of $\Omega = 0.05$ are slightly twisted.

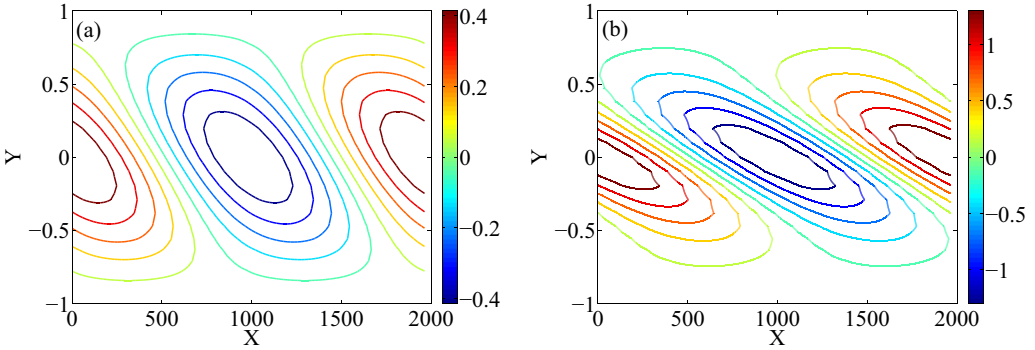

FIG. 9. (Color online) Contour plot of the optimal perturbation $v^{\text{opt}}(x, y, z = 0)$ for (a) $\Omega = 0$ and (b) $\Omega = 0.05$. The Reynolds number is $\text{Re} = 20\,000$. The wave numbers are the ones giving the optimal transient growth.

TABLE I. Existing experimental setups of plane Couette flows and their onset of linear instability under earth's rotation. The value Re^c is computed according to $\mathrm{Re}^c \simeq 1800\ \Omega^{-1}$, while $d^\star$ corresponds to the gap distance beyond which the linear instability sets in before the nonlinear transition to turbulence in PCF.

Place	Gap d (mm)	Ω	$\mathrm{Re}^{c,\mathrm{linear}}$	$d^\star$ (mm)
Toronto [20]	58	0.169	10651	234.8
Stockholm [21]	10	0.006	3×10^5	214.8
Paris [22]	7	0.003	6×10^5	212.7
Zürich [23]	31.2	0.052	34615	227.7

V. CONCLUSION

We presented in this paper a study of the linear stability and transient energy growth in rotating plane Couette flows, where the rotation axis is perpendicular to the planes. Such a rotating framework is of interest to geophysical and astrophysical flows. For example, plane Couette and Taylor-Couette experiments that are often used to study the stability of geophysical and astrophysical flows [10] are all exposed to the earth's rotation. By linearizing the Navier-Stokes equations, we computed the neutral stability curve dividing the linearly stable and unstable regions in the Re-Ω parameter space. Three different types of instabilities are found: for $\Omega > 20$, type I and type II instabilities, which are already known from the Ekman boundary layer flow, and for $\Omega < 20$, type 0 instabilities. The results are consistent with the previous one reported in [3,4]. Moreover, we found that the critical Re for $\Omega < 5$ scales as a power law with Ω, $\mathrm{Re}^c(\Omega) \simeq 1800\ \Omega^{-1}$, which agrees with the fact that the PCF ($\Omega = 0$) is linearly stable for all Re.

Through computation of the eigenvalues and eigenfunctions of the governing linear operator L, we obtained the global optimal transient growth in the α-β plane among all possible initial perturbations. Our results show that the external rotation can have both enhancing and suppressing effects on the optimal transient growth. For weak rotation, it increases the transient growth, while strong rotation significantly inhibits the transient growth. At the rotation numbers relevant for geophysical applications, for example, the atmospheric boundary layer, the transient growth is so small that linear stability analysis appears to be the appropriate tool to determine the stability limits of Ekman layers in the geophysical context. At small rotation the optimal growth scales slightly faster than the power law Ω^2 as is found in plane Couette flow. Furthermore, the wave numbers where the optimal transient growth is obtained are also different from the nonrotating case. The optimal wave number α stays the same, scaling as a power law $\alpha \sim \mathrm{Re}^{-1}$, whereas the optimal wave number β is shifted linearly with Re.

The rotation of the earth mostly has been intuitively considered to be too weak to influence the experiments qualitatively. However, our results tell us that in the case of PCF the earth's rotation changes radically the flow stability, from linearly stable to linearly unstable. This instability may be attributed to the inflection points in the base velocity profile introduced by the external rotation. Table I lists the existing experimental PCF setups and their approximate critical Reynolds number for the linear instability under earth's rotation. The value $d^\star$ indicates a reference gap distance where $\mathrm{Re}^{c,\mathrm{linear}} = \mathrm{Re}^{c,\mathrm{nonlinear}}$, i.e., the critical Reynolds number from the linear instability equals the one computed from the nonlinear mechanism in PCF ($\sim$650 based on the gap distance; see [22,24,25]). Although the linear Re^c are far beyond the onset of turbulence via nonlinear mechanism, the results provide important theoretical guidance for the design of future PCF setups. It may also be relevant to recent Taylor-Couette studies at Re of order 10^6 [10–12] in that at large Re the additional component of rotation induced by the earth's rotation may also cause inflection points in the base velocity profile. Further studies on the underlying physical mechanisms will contribute to the understanding of shear flows in rotating frameworks.

ACKNOWLEDGMENTS

L.S. appreciates fruitful discussions with Professor Marc Avila and Dr. Xing Wei. We acknowledge the research funding by Deutsche Forschungsgemeinschaft under Grant No. SFB 963/1 (project A8) and the support from the Max Planck Society.

[1] F. Rincon, G. I. Ogilvie, and C. Cossu, Astron. Astrophys. **463**, 817 (2007).
[2] T. Tsukahara, N. Tillmark, and P. H. Alfredsson, J. Fluid Mech. **648**, 5 (2010).
[3] N. Hoffmann, F. H. Busse, and W. L. Chen, J. Fluid Mech. **366**, 311 (1998).
[4] Y. Ponty, A. D. Gilbert, and A. M. Soward, J. Fluid Mech. **487**, 91 (2003).
[5] A. A. Draad and F. T. M. Nieuwstadt, J. Fluid Mech. **361**, 297 (1998).
[6] E. Brown and G. Ahlers, Phys. Fluids **18**, 125108 (2006).
[7] J. Boisson, D. Cébron, F. Moisy, and P. P. Cortet, Europhys. Lett. **98**, 59002 (2012).
[8] S. A. Triana, D. S. Zimmerman, and D. P. Lathrop, J. Geophys. Res.: Solid Earth **117**, B04103 (2012).
[9] S. Balbus, Nature (London) **470**, 475 (2011).
[10] H. Ji, M. Burin, E. Schartman, and J. Goodman, Nature (London) **444**, 343 (2006).
[11] E. Schartman, H. Ji, M. Burin, and J. Goodman, Astron. Astrophys. **543**, A94 (2012).
[12] M. S. Paoletti and D. P. Lathrop, Phys. Rev. Lett. **106**, 024501 (2011).
[13] M. Avila, Phys. Rev. Lett. **108**, 124501 (2012).
[14] S. C. Reddy and D. S. Henningson, J. Fluid Mech. **252**, 209 (1993).
[15] S. A. Orszag and L. C. Kells, J. Fluid Mech. **96**, 159 (1980).
[16] P. G. Drazin and W. H. Reid, *Hydronamic Stability* (Cambridge University Press, Cambridge, 1981).
[17] D. K. Lilly, J. Atmos. Sci. **23**, 481 (1966).
[18] K. M. Butler and B. F. Farrell, Phys. Fluids A **4**, 1637 (1992).

[19] W. H. Press, S. A. Teukolsky, W. T. Vetterling, and B. P. Flannery, *Numerical Recipes: The Art of Scientific Computing* (Cambridge University Press, Cambridge, 2007).
[20] E. M. Aydin and H. J. Leutheusser, Exp. Fluids **11**, 302 (1991).
[21] N. Tillmark and P. H. Alfredsson, J. Fluid Mech. **235**, 89 (1992).
[22] S. Bottin and H. Chaté, Eur. Phys. J. B **6**, 143 (1998).
[23] D. Krug, B. Lüthi, H. Seybold, M. Holzner, and A. Tsinober, Exp. Fluids **52**, 1349 (2012).
[24] Y. Duguet, P. Schlatter, and D. S. Henningson, J. Fluid Mech. **650**, 119 (2010).
[25] L. Shi, M. Avila, and B. Hof, Phys. Rev. Lett. **110**, 204502 (2013).